

Hartree-Fock+BCS Approach to Unstable Nuclei with the Skyrme Force

Naoki TAJIMA^{*)}

Department of Applied Physics, Fukui University, Fukui 910-8507, Japan

(Received)

We reanalyze the results of our extensive Hartree-Fock + BCS calculation from new points of view paying attention to the properties of unstable nuclei. The calculation has been done with the Skyrme SIII force for the ground and shape isomeric states of 1029 even-even nuclei ranging $2 \leq Z \leq 114$. We also discuss the advantages of the employed three-dimensional Cartesian-mesh representation, especially on its remarkably high precision with apparently coarse meshes when applied to atomic nuclei. In Appendices we give the coefficients of finite-point numerical differentiation and integration formulae suitable for Cartesian mesh representation and elucidate the features of each formula and the differences from a method based on the Fourier transformation.

§1. Introduction

Among theoretical attempts which aim at treating all the nuclides in a single framework, the simplest category seems to be the mass formula. Hence, let us focus on the nuclear masses in the first place, although the scope of this paper is not restricted to the masses. The most familiar mass formula is certainly that of Bethe and Weizsäcker,^{1),2)} which expresses the nuclear masses as a function of the number of neutrons (N) and that of protons (Z) as,

$$E(N, Z) = a_V A + a_S A^{2/3} + a_I (N - Z)^2 A^{-1} + a_C Z^2 A^{-1/3}, \quad (1.1)$$

where $A = N + Z$ is the mass number. The four terms on the right-hand side of this equation are called respectively the volume, the surface, the symmetry and the Coulomb terms. These terms come from the liquid-drop picture of the atomic nucleus, in which the density distribution of nucleons is assumed to be spatially uniform inside nuclei and the uniform density value is common to all the nuclei.

Incidentally, it is worth stressing that even the form of the symmetry term is completely understandable within the liquid-drop picture. It is not necessary to bring up the Fermi gap model like, e.g., in p. 5 of Ref.³⁾ The form of this term can be naturally derived for a liquid drop by admitting that the coefficient of the volume term should have a dependence on the ratio of the constituents. Because one knows that the volume energy becomes maximum when the proportion of protons (or neutrons) is 50%, the volume term should be modified as,

$$a_V A \longrightarrow \left\{ a_V + a'_V \left(\frac{1}{2} - \frac{Z}{A} \right)^2 \right\} A = a_V A + \frac{a'_V (N - Z)^2}{4A}, \quad (1.2)$$

^{*)} E-mail address: tajima@quantum.apphy.fukui-u.ac.jp

if one retains terms only up to the second order in Z/A . On the right-hand side of this equation, the first term is the original volume term and the second term is identical to the symmetry term by rewriting $\frac{1}{4}a'_V = a_I$. If one applies a similar consideration to the surface term one obtains a so-called surface symmetry term, $a'_I(N - Z)^2 A^{-4/3}$. This term is sometimes added to the liquid-drop mass formula of Eq. (1.1) recently.

Now, by changing the values of the four coefficients (a_V , a_S , a_I and a_C), the root-mean-square (r.m.s.) error from all the experimental data of about 2,000 even-even nuclei available at present^(4),5) can be decreased down to 3.5 MeV. Inclusion of the surface symmetry term can decrease the error further. The accuracy of 3.5 MeV is very small compared with the binding energies of heavy nuclei (~ 1 GeV). However, the requirement for theoretical predictions of the energies of unknown nuclei is something more precise. The separation energy of a neutron, S_n , decreases as the neutron number N is increased. Its changing rate can be roughly estimated to be

$$\frac{\partial S_n}{\partial N} \simeq -\frac{20}{(N^2 A)^{1/3}} \text{ (MeV)} = -\frac{26}{A} \text{ (MeV, for } N = \frac{2}{3}A), \quad (1.3)$$

of which the right-hand side of the first (approximate) equality is the reciprocal of the single-particle level density at the Fermi level obtained by assuming a harmonic oscillator potential with $\hbar\omega_{\text{osc}} = 41A^{-1/3}$ MeV. The right-hand side of the last equality, which is the expression for nuclei on the neutron drip line, becomes as small as 100 keV for the heaviest nuclei. It means that the precision of mass predictions must be 100 keV in order to predict the location of the neutron drip line.

The first step to decrease the error is to take into account the shell effect. For example, the TUYU mass formula⁽⁶⁾ achieved an r.m.s. mass error of 538 keV. The number of fitting parameters are 6 for the gross part (corresponding to the parameters of the Bethe-Weizsäcker formula) while that for the shell part is as many as 269: There is one parameter for each value of Z in an interval $1 \leq Z \leq 112$ and one for each value of N in $1 \leq N \leq 157$. Generally speaking, less number of parameters are preferable for the reliability of the extrapolation to nuclei not synthesized yet. One usually switches to less phenomenological models in order to reduce the number of parameters.

What should be considered next is that the shell effect is strongly dependent on deformation. Indeed, the research group which presented the TUYU mass formula has started the development of a new method which includes the concept of deformation.^(7),8) Of course there are different directions to proceed. For example, a model based on the shell-model configuration mixing has achieved an r.m.s. error of 375 keV with 28 parameters.⁽⁹⁾ The latest good review on the methods of theoretical predictions of nuclear masses can be found in Ref.⁽¹⁰⁾

The most elaborately developed model which takes into account deformation seems to be the finite-range droplet model with a microscopic shell correction (FRDM), whose latest update was done by Möller et al.⁽¹¹⁾ Another extensive calculation was carried out by Aboussir et al.⁽¹²⁾ in the extended Thomas-Fermi plus Strutinsky integral method (ETFSI).

These two methods can be regarded as approximations to the Hartree-Fock (HF)

method. The straight-forward solutions of the HF equations including deformation require long computation time even with present computers in order to cover thousands of nuclei. We understand that the first calculation of such a large scale which have been published is our calculation¹³⁾ done in the framework of the HF+BCS method with the Skyrme SIII force. After the publication of our paper,¹³⁾ only a few similar extensive calculations have been done. Tondeur et al. have performed a set of such extensive calculations in the framework of the HF+BCS and proposed a new Skyrme force parameter set MSk7 best suited for their truncated oscillator basis.^{14),15)} Another attempt have been carried out in the relativistic mean-field framework.¹⁶⁾

In section 2, we discuss about the Cartesian mesh representation of the wave functions, which is a feature of our calculations. Details not included in Ref.¹³⁾ are relegated to the Appendices.

In section 3, we reanalyze the results of our extensive calculation in order to give discussions from new points of view and to compare the results with those of other models.

§2. Cartesian-Mesh Representation

The most usual method to solve the mean-field equations without assuming the spherical symmetry is to expand single-particle wave functions in terms of truncated anisotropic harmonic-oscillator basis.^{17),18)} Instead, we employ a three-dimensional Cartesian-mesh representation:¹⁹⁾ We put a nucleus in a box containing $\sim 10^4$ mesh points and express each single-particle wave function in terms of its values at the mesh points. The advantages of this representation can be summarized as follows:

(1) It has no prejudice concerning the shape of the nucleus. On the other hand, in methods based on expansions in the anisotropic oscillator basis, the shape of the solution should be similar to that of the basis in order that the truncation of the basis does not affect the solution. To fulfill this requirement, one usually solves the mean-field equation imposing constraints on the quadrupole moments such that the resulting shape agrees with the anisotropy of the basis. Then, to obtain the ground state, one has to optimize the anisotropy of the basis such that the energy of the solution is minimized. This procedure is not only cumbersome but also unmanageable in treating exotic states: For example, if the protons and the neutrons may have different shapes, the dimension of the parameter space for the optimization is squared. On the other hand, in the mesh representation, one can treat various shapes with the same mesh. Consequently, the optimization procedure is not necessary.

(2) In the mesh representation the asymptotic form of the wave function at large radius can have arbitrary form, while in the oscillator basis representation it must have a Gaussian tail and therefore loosely bound single-particle wave functions like neutron halo²⁰⁾ cannot be correctly described.

(3) Among systems of many particles found in nature, the atomic nucleus is a very suitable object to apply the Cartesian-mesh representation: Inside nuclei, the density is roughly constant and therefore the local Fermi momentum is also

constant everywhere. This situation favors an expansion in the plane wave basis, to which the Cartesian mesh representation can be an accurate approximation by using appropriate approximation formulae for derivatives and integrals as discussed in Appendices. Consequently, apparently coarse meshes can result in unexpectedly high precision: With mesh spacing $a \sim 1$ fm, there are only a few mesh points in the surface region. Nevertheless, the relative error of the total energy and the quadrupole moment with this mesh spacing is as small as 0.5 % for heavy nuclei. The left-hand portion of Fig. 1 shows how the total energy of ^{170}Er changes as a function of the mesh spacing. At $a=1$ fm, the error is ~ 7 MeV, which is indeed small (0.5%). Furthermore, as shown in the right-hand portion of the figure, the energy difference between prolate and oblate solutions is by far more precisely determined (error ~ 0.4 MeV) with $a=1$ fm. Owing to this independence of the error from the shape, we have found it possible to correct the total energy by adding a simple function of only Z and N to decrease the error down to ~ 0.2 MeV

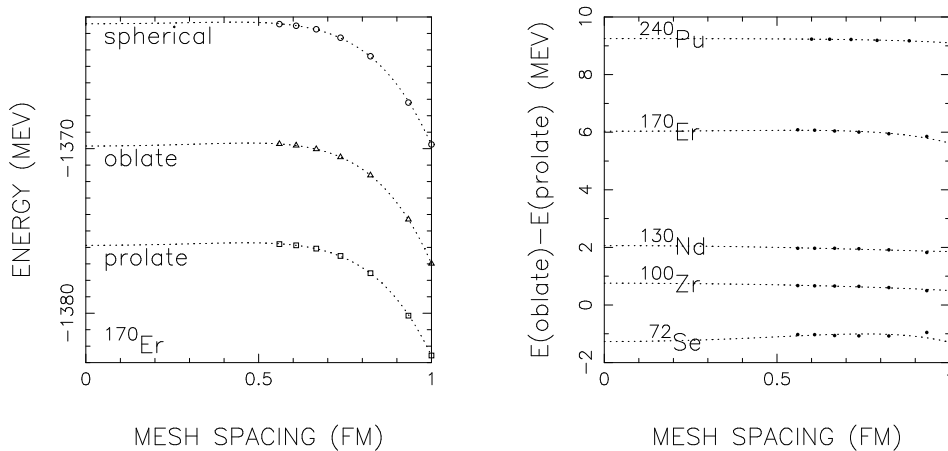


Fig. 1. Left-hand portion shows the total energy of ^{170}Er (for the prolate minimum, the oblate minimum, and the spherical saddle point) versus mesh spacing a . The circles, triangles, and squares are the results of calculations while the curves represent functions $E = c_0 + c_2 a^2 - c_6 a^6$ where c_i are determined through least-square fittings. Right-hand portion gives the energy difference between prolate and oblate minima for five nuclei.

(4) The algorithm of the calculation is simple. This simpleness increases the reliability of computer programs based on the algorithm. It also makes the programs efficiently executable with vector-processor type computers. The programs can also be fitted to each unit of massively parallel computers because the necessary memory is not huge.

§3. HF+BCS Calculations with the Skyrme Force

Using the Cartesian mesh representation, we have calculated the ground and shape isomeric states of even-even nuclei with $2 \leq Z \leq 114$ and N ranging from outside the proton drip line to beyond the experimental frontier in the neutron-rich side. We have obtained spatially localized solutions for 1029 nuclei, together with

the second minima for 758 nuclei. Details not described in this paper can be found in Refs.^{13), 21), 22)}

The Skyrme force^{23), 24)} is an effective interaction widely used in mean-field calculations. It is essentially a zero-range force but modified with the lowest order momentum dependences to simulate the finite-range effects, a density dependence to reproduce the saturation, and a spin-orbit coupling term. The SIII²⁶⁾ is one of the many parameter sets proposed for the Skyrme force. It features good single-particle spectra and accurate $N - Z$ dependence of the binding energy.²⁵⁾

We have used a computer program named *EV8*.¹⁹⁾ In the program, one places an octant of a nucleus in a corner of a box ($13 \times 13 \times 14 \text{ fm}^3$ for $Z \leq 82$ and $14 \times 14 \times 15 \text{ fm}^3$ for $Z > 82$), imposing a symmetry with respect to reflections in x - y , y - z , and z - x planes (the point group D_{2h} ²⁷⁾). The mesh spacing is 1 fm as explained in the last section.

For the pairing, we employ a seniority force, whose pair-scattering matrix elements are defined as a constant G_τ (τ distinguishes between proton and neutron) multiplied by a cut-off factor which is a function of the single-particle energy ϵ . The cut-off is set at $\epsilon = (\text{Fermi level} + 5 \text{ MeV})$ with smearing width of 0.5 MeV. For neutrons, the cut-off function is multiplied furthermore by $\theta(-\epsilon)$. The strength G_τ is determined for each nucleus such that the continuous spectrum approximation using the Thomas-Fermi single-particle level density reproduces the classical empirical formula $\Delta = 12 \text{ MeV}/\sqrt{A}$.

Since the pairing correlation has strong influences on deformations, one must not trifle the choice of the pairing force if one wants to perform deformed mean-field calculations. Our treatment is simple in the sense that it employs the seniority force but it is an advanced treatment in the sense that the force strength is determined as a function of the size of the configuration space for the pairing correlation.

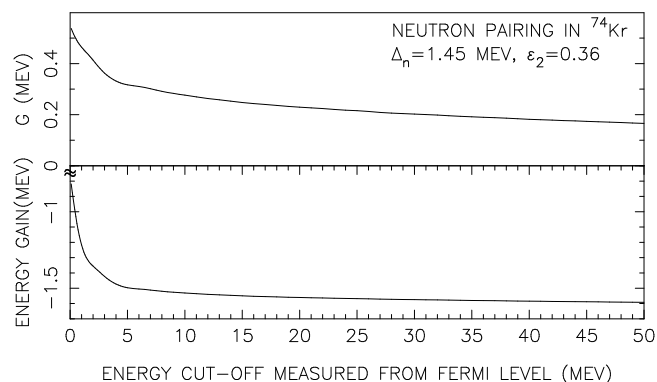


Fig. 2. Dependence of the seniority pairing force strength G renormalized in such a way that the resulting pairing gap agrees with the experimental value (top portion) and the dependence of the energy gain due to the pairing correlation calculated with the strength G (bottom portion) on the cut-off energy. Single-particle levels of the Nilsson potential are used in the BCS calculation.

It is important not to include positive energy neutron orbitals in BCS calculations. Otherwise the resulting density distribution has unphysical neutron gas spreading over the normalization box. For neutron-rich nuclei in which the Fermi

level is not far from zero energy, the pairing configuration space restricted to negative-energy HF orbitals becomes too small to obtain a reliable result within the BCS scheme.

Figure 2 shows the results of a test calculation to illustrate the inadequacy of too small pairing spaces for BCS calculations. The calculation is done using the single-particle spectrum of the Nilsson model, which does not include the continuum spectrum and free from the problem of the formation of the unphysical neutron gas. The strength G of the seniority pairing force is determined in such a way that, for each value of the cut-off (measured from the Fermi level), the neutron's pairing gap Δ_n calculated within the BCS scheme agrees with the experimental value of 1.45 MeV. The value of thus defined strength G is shown in the upper half portion of Fig. 2. The bottom half portion shows the energy gain due to the pairing correlation calculated with the value of G shown in the top portion. The energy gain does not change sizeably for the cut-off energy greater than ~ 4 MeV. For cut-offs less than that value, however, the energy gain is non-negligibly smaller than the values calculated with enough large cut-offs.

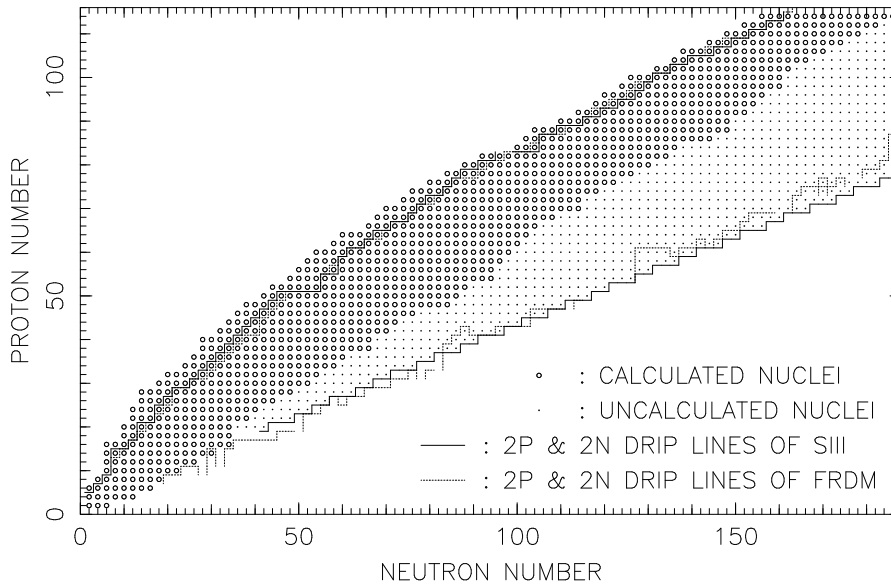


Fig. 3. Even-even nuclei covered by our extensive calculation (open circles). Dots are the uncalculated even-even nuclei between the drip lines. Two-proton and two-neutron drip lines are drawn with solid lines. Dot lines are those from the results of FRDM.¹¹⁾

From the above consideration concerning the effect of the continuum states on the neutron's pairing correlation, it is not very meaningful to apply the HF+BCS scheme to nuclei in which the Fermi level of neutrons is higher than ~ -4 MeV. Thus we restrict our calculation within only several neutrons beyond the experimental neutron-rich frontier. Figure 3 shows thus selected even-even nuclei. The two-proton drip line (the upper one of the solid lines) is deduced from the total energies of our HF+BCS calculation. Solution of nuclei outside the proton drip line can be obtained owing to the Coulomb barrier. The two-neutron drip lines (the lower one of the solid

lines) is obtained from the Bethe-Weizsäcker type mass formula of Eq. (1.1) whose four coefficients are determined through a least-square fitting to the total energies from our HF+BCS calculation. One can see that roughly half of the even-even nuclei are included in our calculation.

In light-mass region, the neutron's Fermi levels of some of the calculated nuclei are higher than -4 MeV. For such nuclei, the renormalized pairing force strength becomes very large. We cut the strength at 0.6 MeV. As a consequence, our solutions for such light-mass nuclei near the neutron drip line do not have pairing correlation.

The current subject of our research is the calculation of the remaining half of the nuclear chart on the neutron rich side by developing a feasible Hartree-Fock-Bogoliubov framework which enables one to include the effect of the Hartree-Fock continuum (states which are in the continuum part of the Hartree-Fock single-particle spectrum) on the pairing correlation. We think it preferable if the wave functions are expressed in the coordinate space with a three-dimensional Cartesian mesh in order to describe possible large surface diffuseness like thick skins and halos as well as arbitrary deformations. A method utilizing the localization of HFB canonical basis seems to be very promising.^{28), 29)}

§4. Analyses of the Results

In this section we reanalyze the results of our extensive HF+BCS calculations,¹³⁾ by presenting the results from new aspects. Note that all the resulting data of our calculations are available on the WEB.¹³⁾ In principle one can reproduce the figures given in this section using only the data on the WEB.

4.1. Mass

Concerning the nuclear masses, the r.m.s. error of our result turns out to be 2.2 MeV, which is not so good as those of the latest mass formulae (typically 0.5 MeV). Note that this was the first published estimation of the r.m.s. mass error of any of the Skyrme forces. It is an interesting question how much the error can be decreased by improving the parameters of the Skyrme force through an extensive fitting to currently available experimental masses.^{14), 15)} To achieve the precision of 100 keV, improvement of the treatment of the pairing is certainly necessary. It may also be necessary to add some new terms to the Skyrme force. Some think that corrections for correlation energies should be included.

Leaving this question which is out of the scope of this paper, let us reanalyze our result from different aspects not taken in Ref.¹³⁾

The top portion of Fig. 4 shows the errors of the calculated masses as a function of the neutron number N . The bottom portion plots the same data versus the proton number Z . Nuclei of $N = Z$ are designated with open circles (appearing in $N, Z < 40$) while the others with dots.

One can see that the $N = Z$ nuclei are always at the highest peaks of the isotope and the isotone chains to which they belong. This means that our mean-field calculation does not have the mechanism corresponding to the Wigner term of the mass formulae. It is now widely understood that the Wigner comes from the

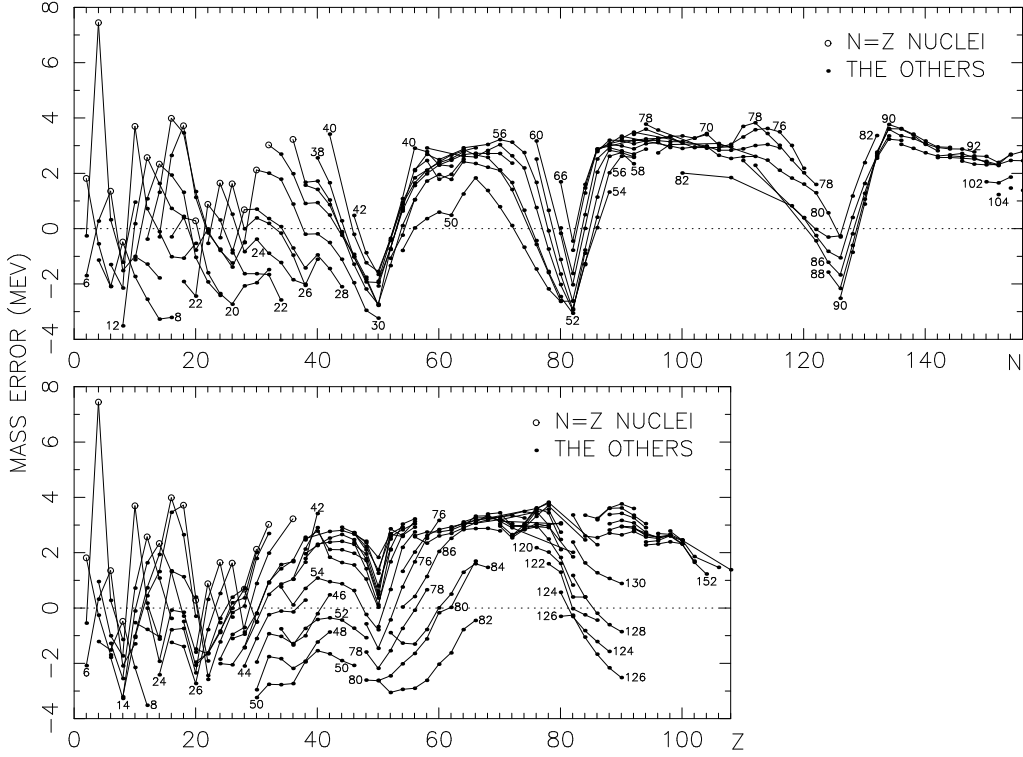


Fig. 4. Errors of the nuclear masses calculated in HF+BCS with Skyrme SIII force plotted as a function of the neutron number N (top portion) and the proton number Z (bottom portion). Isotopes and isotones are connected with lines. The number printed near each line of isotope or isotone chain means the proton or neutron number of the chain.

$T = 0$ pairing. On the other hand, in the present HF+BCS approach the pairing correlation is considered only between like nucleons, which means a $T = 1$ pairing.

The behavior of the errors looks very systematic in region $Z, N > 40$ compared with in lighter-mass region. One can see from the top figure that mass difference becomes minimum (i.e., the calculated values are more bound than experimental values) always at neutron's spherical magics of $N = 50, 82$, and 126 . The situation is less clear in the bottom figure, but at least a spherical magic of protons, $Z = 50$, is a minimum of the isotone chains except for the $N = 82$ chain. This observation suggests that the employed force has too large a stiffness against deformation.

Concerning the possibly too large surface tension of the employed force, Fig. 5 plots the errors of the calculated nuclear masses divided by $A^{2/3}$ (which is proportional to the error per unit surface area) versus $B_{\text{surf}} - 1$, where B_{surf} is the ratio of the surface area to that of the spherical shape. The increase of the surface energy due to deformation is proportional to $B_{\text{surf}} - 1$. The surface area is calculated using liquid-drop shape parameters, whose definition in term of moments is given later in the next subsection. The error is negative for half of the spherical nuclei ($B_{\text{surf}} = 1$), while for deformed nuclei it is roughly constant and independent of B_{surf} (i.e., the size of deformation). The situation is also independent of whether the nucleus is light

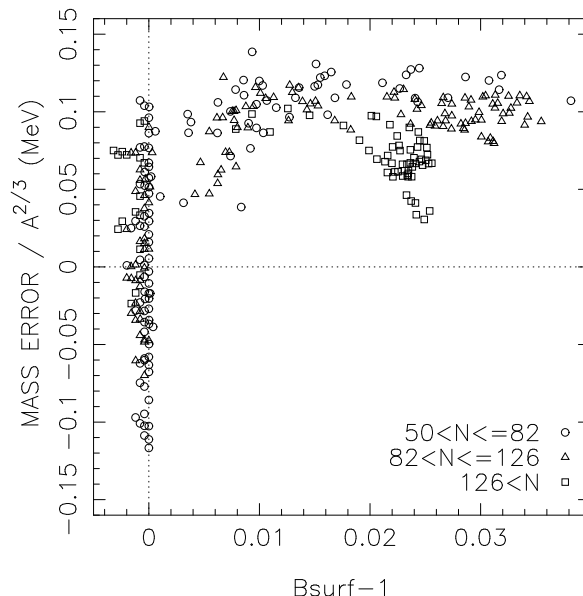


Fig. 5. Errors of nuclear masses divided by a mass-number dependence factor $A^{2/3}$ as a function of the surface factor B_{surf} subtracted with 1. Open circles, triangles, and squares are used for the sake of distinction of the heaviness of the nuclei. The symbols in the left-hand side of the vertical dot line $B_{\text{surf}} - 1 = 0$ should be regarded as on the line: They are shifted to the left only to avoid clustering of too many symbols.

or heavy as one can see three kinds of symbols (circles, triangles, and squares) mixed up in the plot. These results do not suggest that the tendency that deformed nuclei have too large masses can be ascribed solely to the surface energy of the employed force.

4.2. Deformation

Fig. 6 shows a comparison between the experimental and the calculated intrinsic quadrupole moments. For each nucleus whose $B(E2; 0^+ \rightarrow 2^+)$ is experimentally known (289 even-even nuclei ranging over $4 \leq Z \leq 98$),³⁰⁾ a dot is marked at a point whose abscissa is equal to the experimental value and its ordinate to the theoretical value calculated in this paper. The agreement between the experiment and the theory is excellent in most cases. Only a few nuclei exhibit large discrepancies. Three such nuclei whose element names are indicated in the graph (^{176}Pt , ^{222}Ra , and ^{222}Th) are around the shape transitional point of their isotope and isotone chains. It is relatively difficult to predict the deformation of shape transitional nuclei.

It has been reported that our results have roughly the same quality as the other principal theoretical approaches concerning the reproduction of experimental quadrupole moments.³¹⁾

Let us define the deformation parameters in terms of multipole moments for the sake of comparison with the results of other models like FRDM and also for the easiness to imagine the shapes. We define the deformation parameters of a HF+BCS solution as those of a sharp-surface uniform-density liquid drop which has the same

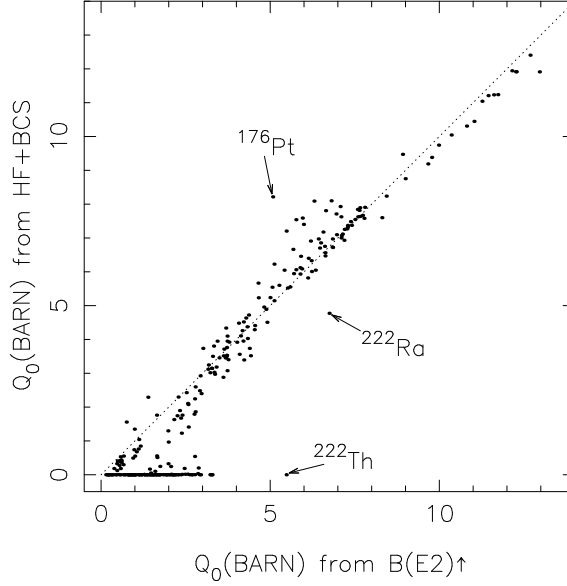


Fig. 6. Comparison of the calculated and experimental quadrupole moment.

mass moments as the solution has. The mass density of the liquid drop is expressed as

$$\rho(\mathbf{r}) = \rho_0 \theta(R(\hat{\mathbf{r}}) - |\mathbf{r}|), \quad R(\hat{\mathbf{r}}) = R_0 \left(1 + \sum_{l=0}^{\infty} \sum_{m=-l}^l a_{lm} Y_{lm}(\hat{\mathbf{r}}) \right), \quad (4.1)$$

where θ is the step (Heaviside) function. The necessary and sufficient conditions on a_{lm} to fulfill the reality of $R(\hat{\mathbf{r}})$ and the D_{2h} symmetry are that l and m are even numbers and $a_{lm} = a_{lm}^* = a_{l-m}$. We set $a_{lm} = 0$ for $l \geq 6$ and determine the remaining seven parameters ρ_0 , R_0 , a_{20} , a_{22} , a_{40} , a_{42} , and a_{44} such that the liquid drop has the same particle number, mean-square mass radius, and mass quadrupole ($r^2 Y_{2m}$) and hexadecapole ($r^4 Y_{4m}$) moments as the HF+BCS solution has.

By using the mass number A and the mass moments, one obtains the deformation parameters to express the shape of the mass distribution. The deformation parameters of proton (neutron) distribution can be calculated in a similar way by using proton (neutron) number Z (N) and the moments of proton (neutron) distribution.

Let us check the adequacy of our definition of the shape parameters by comparing them with model-independent quantities.

In the left-hand portion of Fig. 7, we show the correspondence between two quantities related to the axially symmetric quadrupole deformation. They are a_{20} and δ , where the latter is defined as

$$\delta = \frac{3\langle Q_z \rangle}{4\langle r^2 \rangle}, \quad Q_z = 2z^2 - x^2 - y^2, \quad r^2 = x^2 + y^2 + z^2. \quad (4.2)$$

The number of plotted points is 5361. Each point is for the deformation of either mass, proton, or neutron distributions of a HF+BCS solution among 1029 ground

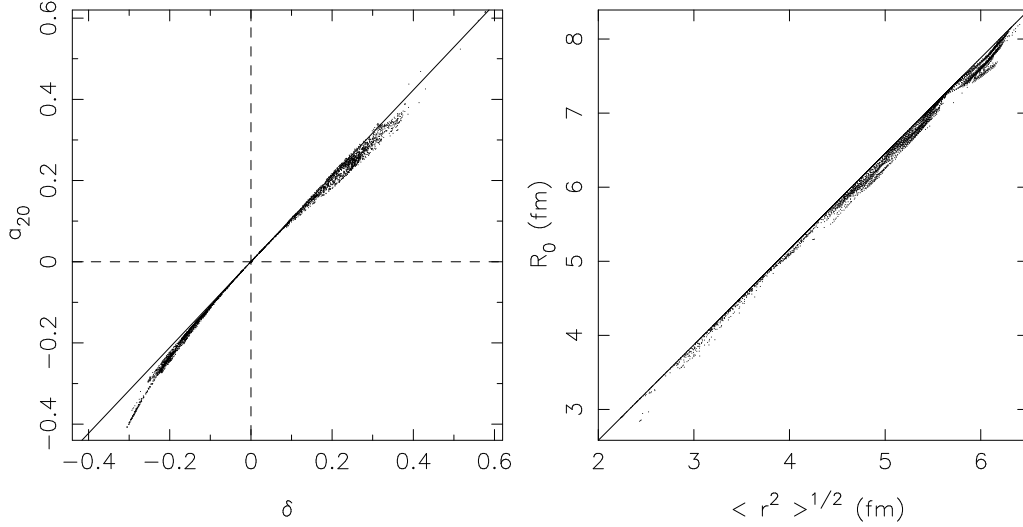


Fig. 7. The correspondence between liquid-drop-model shape parameters and the related model independent quantities. The left-hand portion is for the axially symmetric quadrupole deformation while the right-hand portion is for the radius.

and 758 first-excited states. The solid line represents $a_{20} = (\frac{16}{45}\pi)^{1/2}\delta$, which is the leading-order expression for sharp-surface density distributions. This is a satisfactory result in the sense that the values of a_{20} are never very distant from the widely used model independent deformation parameter δ . We have least-square fitted a polynomial through order three with the leading order coefficient frozen at the above value. The resulting polynomial is $a_{20} = (\frac{16}{45}\pi)^{1/2}\delta - 0.47\delta^2 + 0.78\delta^3$. The maximum and the r.m.s. deviations from this polynomial are 0.05 and 0.007, respectively.

In the right-hand portion of Fig. 7, we plot the liquid-drop-model radius R_0 versus the r.m.s. radius $r_{\text{rms}} = \langle r^2 \rangle^{1/2}$. The diagonal solid line is $R_0 = (\frac{5}{3})^{1/2}r_{\text{rms}}$, which is a relation expected to a spherical liquid drop. It is again a desirable result that the deviations from this line are never be very large. Owing to deformations and the surface diffuseness, R_0 is likely to be slightly smaller than $(\frac{5}{3})^{1/2}r_{\text{rms}}$. For the plotted 5361 points, the maximum and the r.m.s. deviations are 0.3 fm and 0.06 fm, respectively.

In Fig. 8, we compare the axial quadrupole deformation parameter a_{20} between present HF+BCS calculation and the results of the FRDM.¹¹⁾

A systematic difference which is most easily noticed is found around $Z \sim N \sim 40$, where the present HF+BCS calculation tends to predict smaller deformations than the FRDM. This is due to the shape coexistence prevailing in this region.

An example of the shape coexistence is given in Fig. 9. For ^{80}Zr , the HF+BCS method with the SIII force (solid curve) predicts three minima which are energetically competing within 0.6 MeV. The order of the energies of these minima can be altered easily by changing the force parameter to SkM^{*32)} (dash curve) or by decreasing the pairing gap by 25% (dot curve).

Another systematic difference which one may notice in Fig. 8 is in a long and narrow region close to the proton drip line with $94 \leq Z \leq 102$, where the FRDM

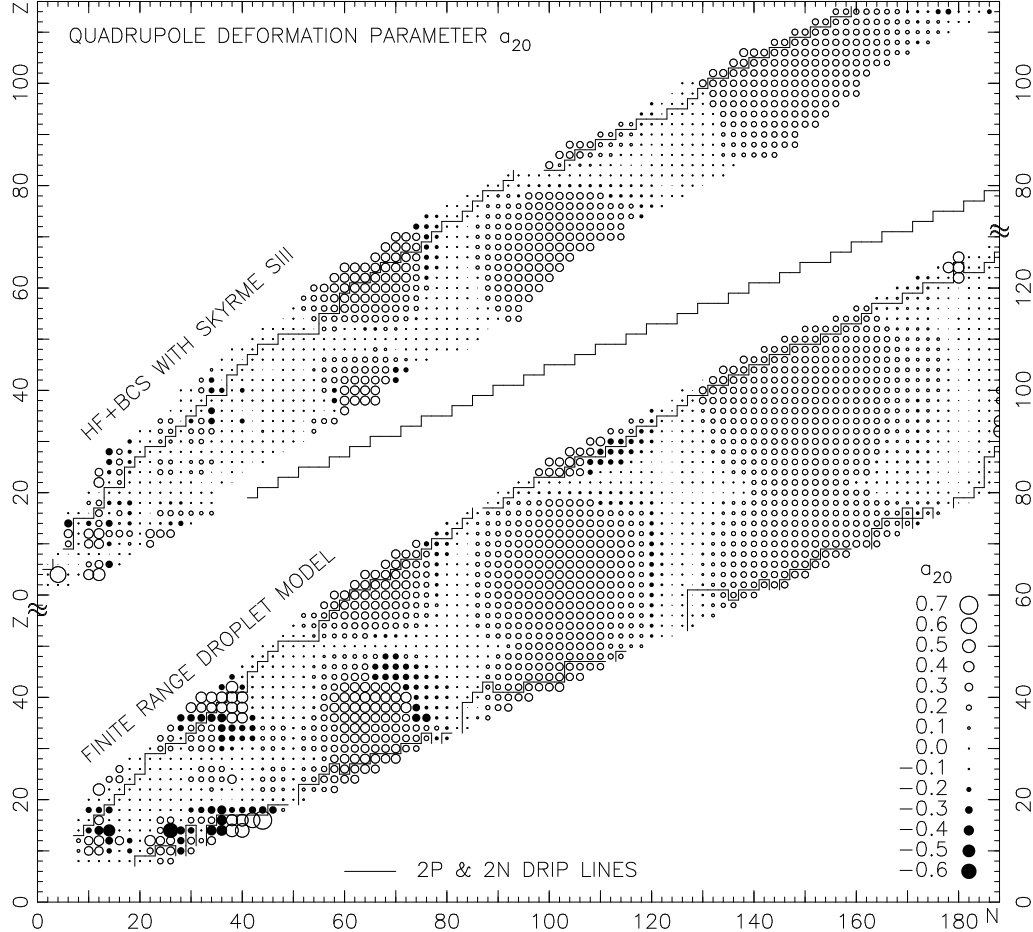


Fig. 8. Comparison of the calculated quadrupole deformation parameter a_{20} between HF+BCS with Skyrme SIII force¹³⁾ and the finite-range droplet model.¹¹⁾ The open (solid) circles designate prolate (oblate) nuclei, while the diameter of the circles is proportional to the magnitude of the deformation parameter. The two-proton and two-neutron drip lines predicted by each model are also drawn.

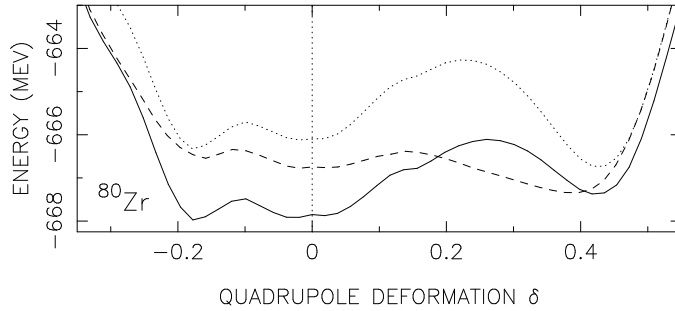


Fig. 9. The Potential energy curve of ^{80}Zr along the axially symmetric quadrupole deformation path. The solid curve is calculated with the SIII force, the dot curve with the SIII force with 25% smaller pairing gap, and the dash curve with the SkM* force.

predicts oblate shapes while our calculations give small-size prolate shapes.

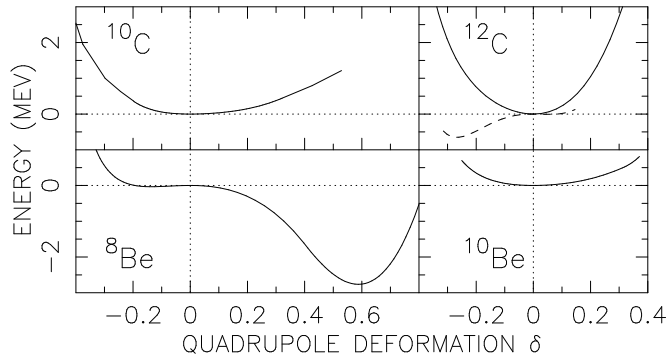


Fig. 10. The potential energy curves for 1p shell even-even nuclei from the HF+BCS with the SIII force. The energy is measured from that of the spherical solution. For ^{12}C the results with the Skyrme SII force is also drawn with dash line.

Figure 10 shows the potential energy curves for $4 \leq Z, N \leq 6$ nuclei, which are obtained with a constraint on the axially symmetric mass quadrupole moment Q_z . The abscissa represents the deformation parameter δ .

Among our calculations for the 1029 even-even nuclei, ^8Be has the largest deformation ($a_{20}=0.62$), which can be explained in terms of the two-alpha-cluster picture. In the bottom-left portion of Fig. 10 one finds the potential energy curve for this nucleus, which exhibits that the deep prolate minimum is the only solution (except for the extremely shallow one at an oblate shape).

For ^{12}C , the experimental $B(E2)\uparrow$ is very large (corresponding to $|a_{20}|=0.59$) and an oblate intrinsic deformation with a triangular three-alpha-cluster configuration has been suggested. However, the HF+BCS calculation gives a spherical ground state. In the top-right portion of the figure we show the potential energy curve, which has only one minimum at the spherical shape. Other widely-used Skyrme forces of the SkM* and the SGII³³⁾ also give the only minimum at sphericity. On the other hand, calculations using the Nilsson model³⁴⁾ and the Strutinski method³⁵⁾ give oblate ground states. An old Skyrme force SII¹⁷⁾ also gives an oblate minimum with $\delta = -0.27$ (the dash curve in the figure).

Concerning ^{10}C and ^{10}Be , the experimental $B(E2)\uparrow$ values indicate large deformations: $|a_{20}|=0.82$ for ^{10}C and 1.1 for ^{10}Be . However, the potential energy curves in Fig. 10 have only the spherical minimum. The quantum fluctuation in shape may be able to account for the large $B(E2)\uparrow$ since the curves are very soft toward prolate deformations.

It is difficult to conclude definitely only from Fig. 10 what deformation ^{12}C should bear in the HF approximation, since the optimal shapes of light nuclei are apt to be changed when effects beyond mean-field approximations are taken into account. The parity projection has been reported to be especially important³⁶⁾ because the triangular three-alpha-cluster configuration violates the symmetry.

Let us briefly report on the three-alpha-cluster linear-chain state of ^{12}C . By extending the potential energy curve in Fig. 10 to larger δ , we have found the first

excited minimum at $\delta \sim 1.0$, in good agreement with the result of the Nilsson model for the linear-chain state ($\delta=1.1$).³⁷⁾ The excitation energy from our calculation is 21 MeV. Though it is much larger than the experimental value of 7.654 MeV, the overestimation will be improved by the angular momentum projection.

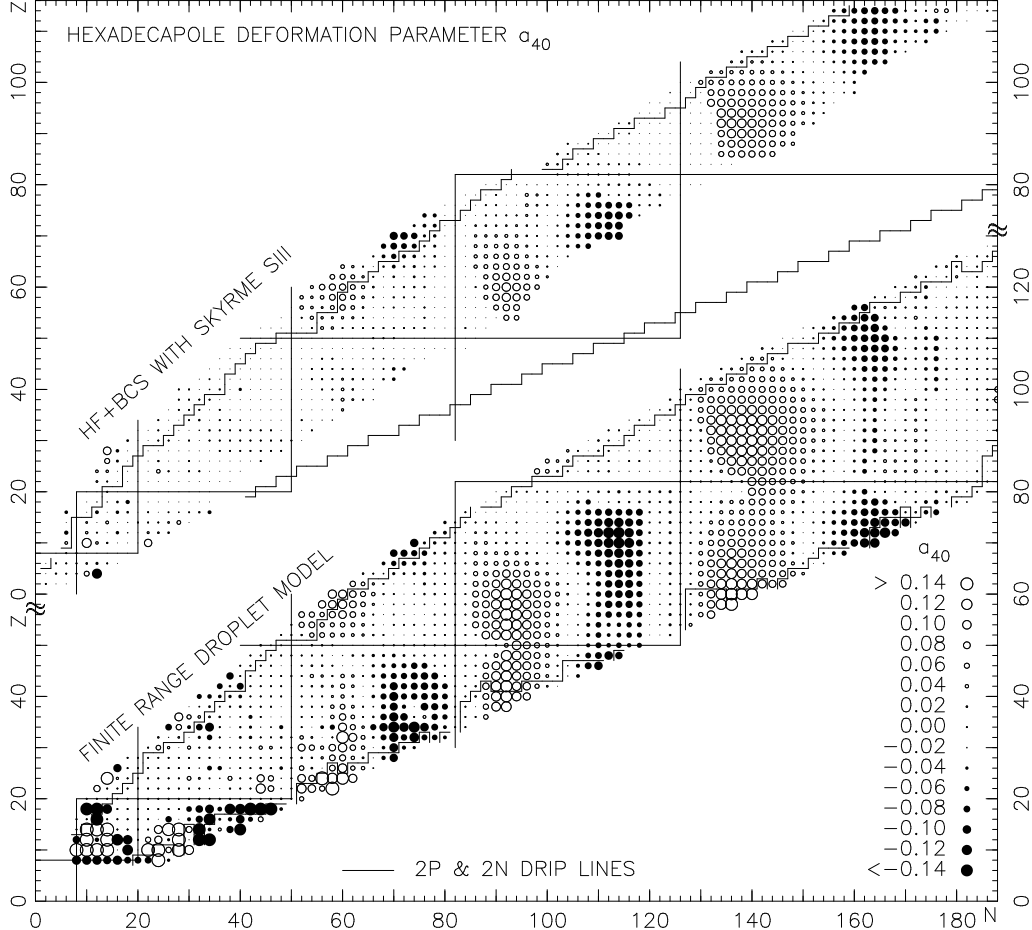


Fig. 11. Same as in Fig. 8, but for the hexadecapole deformation parameter a_{40} . The grid indicates the locations of the magic numbers for spherical shapes. The results of FRDM is taken from Ref.¹¹⁾

In Fig. 11, we compare the axially symmetric hexadecapole deformation parameter a_{40} between the present HF+BCS calculation and the FRDM result.¹¹⁾ A common feature between the results of the two models is that the sign of a_{40} is positive in the bottom-left quarter of the major shells and negative in the top-right quarter. This behavior is perfectly understandable in terms of the density distribution of pure- j single-particle wave functions. A systematic difference between two calculations is found in $Z, N < 50$ where $|a_{40}|$ is very small with exception of only several nuclei in the HF+BCS while it has certain sizes in many nuclei according to the FRDM. In particular, most of the light nuclei with $N, Z < 20$ have conspicuously large $|a_{40}|$ in FRDM. For heavier nuclei, too, the magnitude of a_{40} is generally smaller

in HF+BCS than in FRDM. Further investigation is necessary to see whether these differences are originated in the different definitions of the shape parameters: In the HF+BCS they are calculated from the moments, while in the FRDM they are the input parameters to specify the shape of the single-particle potential.

One of the advantages of mean-field methods over shell-correction schemes is that the protons and the neutrons do not have to possess the same radius and deformation. Indeed, it is one of the reasons to adopt the Cartesian-mesh representation rather than the expansion in harmonic-oscillator bases. In order to make the best use of this advantage, we have calculated the liquid-drop shape parameters separately for protons and neutrons for 1029 ground and 758 first-excited solutions.

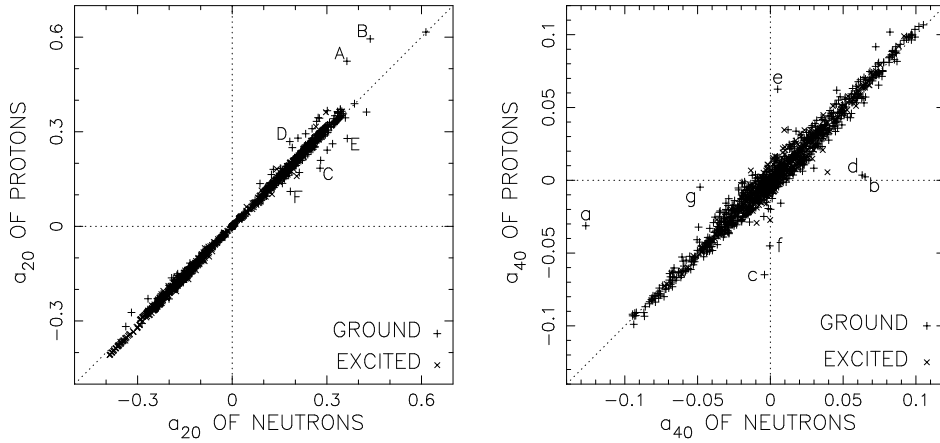


Fig. 12. Difference of the shape parameters between protons and neutrons for the ground states of 1029 even-even nuclei (denoted by plus symbols) and the first-excited solutions (denoted by cross symbols) of 758 even-even nuclei for HF+BCS with SIII force. The left and the right portions show respectively the quadrupole deformation parameter a_{20} and the hexadecapole deformation parameter a_{40} .

The left-hand portion of Fig. 12 presents a comparison of the values of a_{20} between protons and neutrons. The r.m.s. value of the difference $|a_{20}^{\text{neu}} - a_{20}^{\text{pro}}|$ is 0.012, while the maximum difference occurs in the ground state of ${}^{14}_4\text{Be}_{10}$ ($a_{20}^{\text{neu}} = 0.36$, $a_{20}^{\text{pro}} = 0.52$), which is indicated by letter **A** in the figure. Symbols indicated by letters from **B** to **F** are the ground states of ${}^{16}_4\text{Be}_{12}$ ($a_{20}^{\text{neu}} = 0.44$, $a_{20}^{\text{pro}} = 0.59$), ${}^{30}_{18}\text{Ar}_{12}$ (0.28, 0.18), ${}^{30}_{12}\text{Mg}_{18}$ (0.18, 0.27), ${}^{36}_{24}\text{Cr}_{12}$ (0.36, 0.28), and ${}^{28}_{18}\text{Ar}_{10}$ (0.18, 0.11), respectively. Among these nuclei, ${}^{30}\text{Ar}$, ${}^{36}\text{Cr}$, and ${}^{28}\text{Ar}$ are outside the proton drip line. The absolute value of the difference is smaller than 0.05 for 98.9 % of the solutions.

The right-hand portion of Fig. 12 is similar to the left-hand portion but for a_{40} . The r.m.s. value of the difference $|a_{40}^{\text{neu}} - a_{40}^{\text{pro}}|$ is 0.0063, while the maximum difference is found in ${}^{16}_4\text{Be}_{12}$ ($a_{40}^{\text{neu}} = -0.127$, $a_{40}^{\text{pro}} = -0.031$), which is indicated with letter **a**. Symbols indicated by letters from **b** to **g** are the ground state solutions of ${}^{14}_4\text{Be}_{10}$ ($a_{40}^{\text{neu}} = 0.065$, $a_{40}^{\text{pro}} = 0.002$), ${}^{18}_{12}\text{Mg}_6$ (-0.004, -0.065), ${}^{22}_{12}\text{Mg}_{10}$ (0.063, 0.004), ${}^{22}_{10}\text{Ne}_{12}$ (0.005, 0.063), ${}^{22}_{16}\text{S}_6$ (0.000, -0.045), and ${}^{18}_6\text{C}_{12}$ (-0.048, -0.005), respectively. Among these nuclei, ${}^{18}\text{Mg}$ and ${}^{22}\text{S}$ are outside the proton drip line.

To summarize, according to the results of our calculations with the Skyrme SIII force, the largest differences between the shapes of proton and neutron density distributions occur in the lightest nuclei. Except for these nuclei, the differences are not remarkably large.

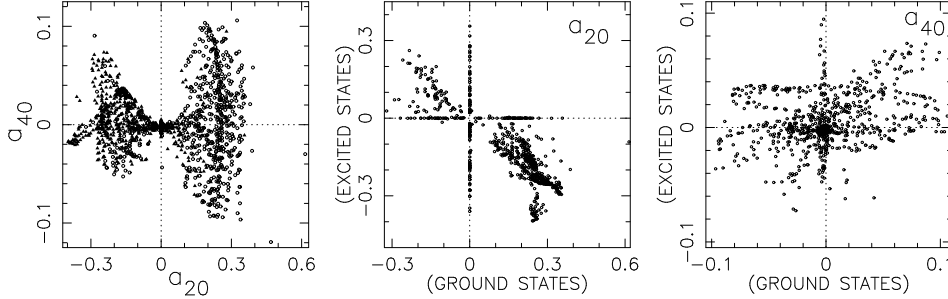


Fig. 13. Correlation between quadrupole and hexadecapole deformation parameters. The left-hand portion shows the relation between a_{20} and a_{40} of each HF+BCS solution. Open circles are for ground state solutions while solid triangles are for the first excited solutions. The middle portion shows the relation between a_{20} of the ground state and a_{20} of the first excited state of a nucleus. An open circle corresponds to a nucleus. Only a kind of symbol is used. Clustering open circles may look like solid circles. The right portion is the same as the middle portion except it is for a_{40} .

In Fig. 13, we investigate the correlations between deformation parameters. The left-hand portion of the figure shows that the ground states (open circles) are mostly with $0.2 < a_{20} < 0.3$ while the excited states (solid triangles) are with $-0.3 < a_{20} < 0$. For prolate ($a_{20} > 0$) states a_{40} ranges from -0.1 to 0.1 while for oblate ($a_{20} < 0$) states a_{40} covers a smaller interval from -0.05 to 0.07 . For nuclei with $a_{20} \sim 0$, a_{40} is also close to zero.

The middle portion of Fig. 13 shows that a_{20} of the ground state of a nucleus and a_{20} of the first excited state of the same nucleus have a strong negative correlation. The most frequent case is that the ground state is prolate and the first excited state is oblate. There are opposite cases, too, but the number is much less. There are also many nuclei in which either ground or the first excited states is spherical ($a_{20} = 0$).

The right-hand portion of Fig. 13 shows that a_{40} have more complicated correlation pattern between ground and the first excited states of a nucleus.

A merit of extensive calculations is that it allows one to see global trends of nuclear properties over the entire area of the nuclear chart. As another example of the analysis of such a global trend, we have investigated the systematics of the energy difference between the oblate and the prolate solutions. In the top portion of Fig. 14, the energy difference is plotted versus the neutron number. One can see an evident difference between below and above the $N = 50$ shell magic: For nuclei with $N < 50$, the oblate solutions often have lower energies than prolate ones. For nuclei with $N > 50$, oblate ground states are very rare and found only in nuclei whose N is slightly smaller than a magic number. In the bottom portion, the same data is plotted versus the proton number Z . One can see that the situation is exactly the same for proton's shell effect.

This abrupt change at $N = 50$ and $Z = 50$ seems to suggest that the dominance

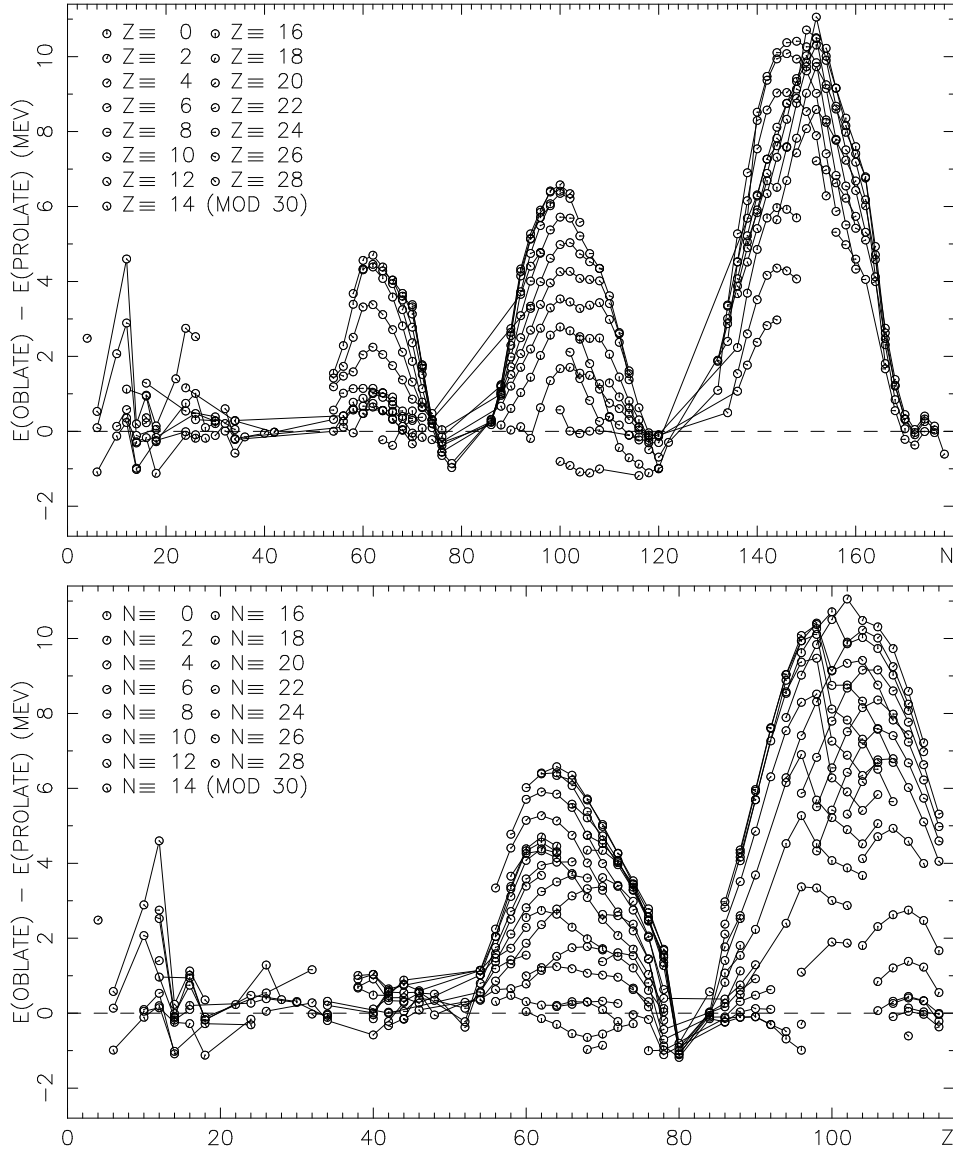


Fig. 14. Energy difference between prolate and oblate solutions. Top and bottom portions show the same results for different abscissae. In the top portion, the abscissa is the neutron number and isotopes are connected with lines. It is possible to read off the proton number of each isotope chain from the direction of the “hand” put in each circle. See the legends in the top-left corner of each portion. In the bottom portion, the abscissa is the proton number and isotones are connected with lines.

of prolate deformations in rare-earth and actinide nuclei may be related with the nature of the Mayer-Jensen major shell while the harmonic-oscillator major shell leads to an equal situation between oblate and prolate deformations. The Mayer-Jensen major shell is composed of the normal parity orbitals which have the same oscillator quantum number and a unique parity orbital which is pushed down from the

next oscillator shell by the spin-orbit potential due to its large angular momentum. We have suggested¹³⁾ that one may ascribe the prolate dominance to the spin-orbit potential.

Recently, we have performed Nilsson-Strutinsky calculations to answer this question.³⁸⁾ The Nilsson potential contains a l^2 potential, which simulates a square-well like radial profile of the mean potential, and a spin-orbit potential. The l^2 potential can reproduce the prolate dominance without the help of the spin-orbit potential, while the spin-orbit potential alone cannot reproduce the prolate dominance. However, this does not mean the weakness of the effect of the spin-orbit potential. On the contrary, it interferes so strongly with the l^2 potential that the ratio of the number of prolate nuclei to that of oblate ones oscillates with a large amplitude, making a prolate dominance with the standard strength, reverting the situation to an oblate-favor one with half the standard strength, and again giving rise to a prolate dominance with vanishing strength.

4.3. Radius

The left-hand portion of Fig. 15 presents a comparison of the liquid-drop radius of protons R_0^{pro} with that of neutrons R_0^{neu} .

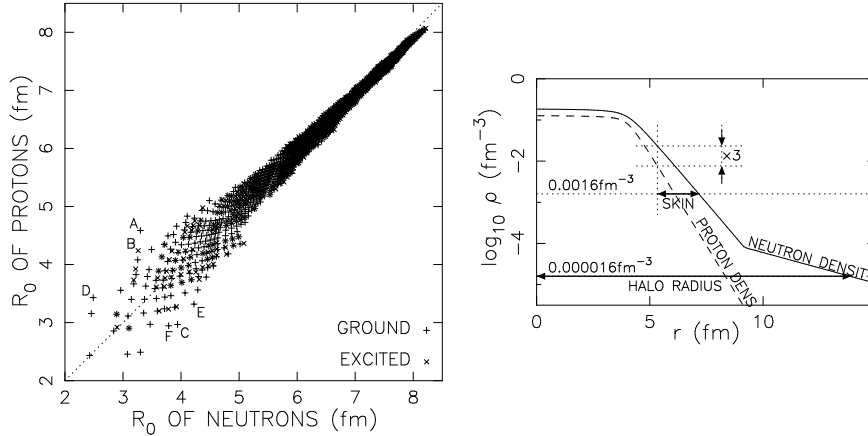


Fig. 15. The left-hand portion shows a comparison of the liquid-drop radius R_0 of the proton distribution and that of the neutron distribution. The right-hand portion shows the definitions employed in this paper of the skin thickness and the halo radius.

The r.m.s. value of the difference $|R_0^{\text{neu}} - R_0^{\text{pro}}|$ is 0.18 fm. Symbols indicated by letters from **A** to **F** are the solutions of ${}^{22}_{16}\text{S}_6$ ($R_0^{\text{neu}} = 3.3$ fm, $R_0^{\text{pro}} = 4.6$ fm), ${}^{20}_{14}\text{Si}_6$ (3.3, 4.2), ${}^{16}_{4}\text{Be}_{12}$ (3.9, 3.0), ${}^8_6\text{C}_2$ (2.5, 3.4), ${}^{22}_{6}\text{C}_{16}$ (4.2, 3.3), and ${}^{14}_4\text{Be}_{10}$ (3.8, 2.9), respectively. Among the nuclei mentioned above, ${}^{20}\text{Si}$ is for the excited state while the others are for the ground states. ${}^{22}\text{S}$, ${}^{20}\text{Si}$, and ${}^8\text{C}$ are outside the proton drip line. Hence the maximum difference for nuclei inside the drip line occurs in the ground state of ${}^{16}\text{Be}$. Incidentally, when we plotted the r.m.s. radii r_{rms} instead of R_0 , we found that the resulting graph looked very similar to this figure except for a constant factor, $R_0 \sim (\frac{5}{3})^{1/2} r_{\text{rms}}$.

Concerning the difference of radial density distribution between protons and

neutrons, one should pay attention not only to volume properties represented by liquid-drop or r.m.s. radius but also to surface properties, which are sensitive to the difference at much lower densities and manifest themselves, e.g., in the thicknesses of nucleon skins and the radii of nucleon halos. The right-hand portion of Fig. 15 is an illustration to explain our definitions of these two quantities. We regard that a point is in the proton skin if $\rho_p > 3\rho_n$ and $\rho_p + \rho_n > 0.0016\text{fm}^{-3}$, where ρ_p and ρ_n are respectively the proton density and the neutron density at that point. A similar definition has been proposed in Ref.³⁹⁾ The halo radius is defined as the radius at which angle-averaged mass density is $1.6 \times 10^{-5} \text{ fm}^{-3}$.

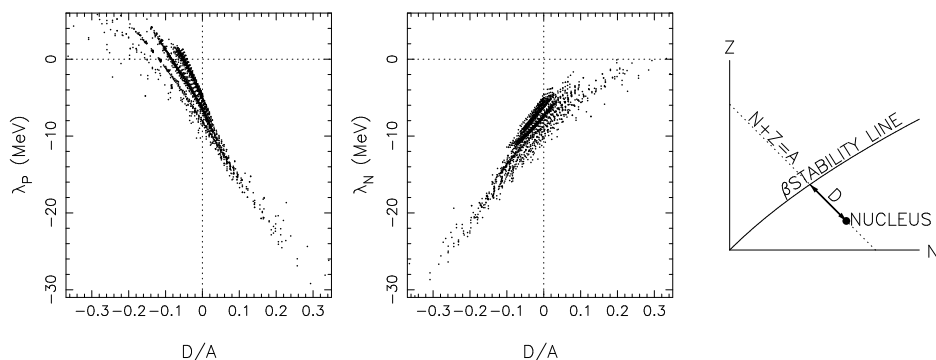


Fig. 16. Fermi levels as functions of the distance from the β -stability line D divided by the mass number A . The left and the middle portions are for protons and neutrons, respectively. The right portion explains the definition of D .

As a preparation before discussing about skins and halos, let us first look at the relation between the Fermi levels and the distance in the (N, Z) plane from the β -stability line. As illustrated in the right-hand portion of Fig. 16, we choose to measure the distance D along a line of constant mass number. We assign a negative sign to D for nuclei with $Z > N$. As the definition of the β -stability line, we employ a classical empirical formula,

$$N - Z = \frac{0.4A^2}{A + 200}, \quad A = N + Z. \quad (4.3)$$

The left- and right-hand portions of Fig. 16 show respectively the Fermi level of the protons λ_p and that of the neutrons λ_n . Both ground-state and first excited solutions are plotted. The abscissa is the distance D divided by the mass number A . One can see a strong correlation in both portions. (Incidentally, the dots spread over larger area if the the abscissa is changed to $DA^{-2/3}$ or $DA^{-4/3}$.) These figures suggest that one can measure the unstableness of a nucleus in two roughly equivalent ways. One may ask how high one of the Fermi levels is instead of asking how far the nucleus is located from the β -stability line in the nuclear chart.

Now, by using the next two figures, we will show that the skin grows monotonously and regularly as nucleons are added to the nucleus while the halo radius grows very slowly except near the drip lines, where it changes the behavior completely and expands very rapidly.

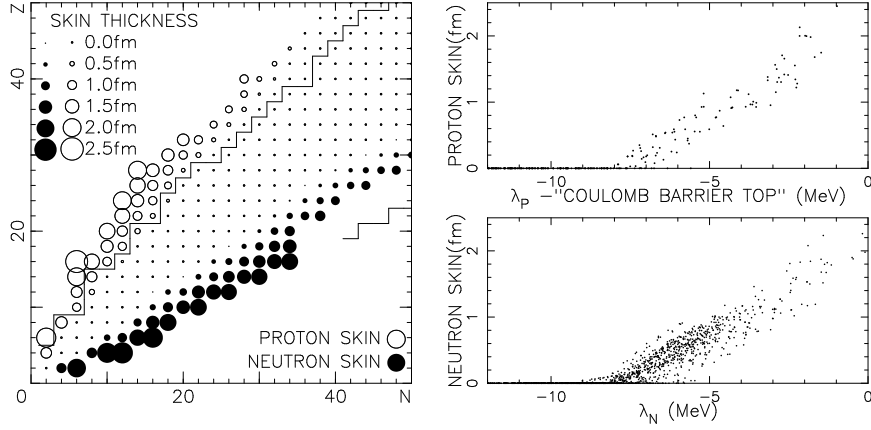


Fig. 17. Skin thickness. In the left portion the thickness of the proton (neutron) skin of the ground states is shown with the radius of open (solid) circles. Nuclei without either type of the skins are shown with the smallest dots. The staircase like lines represent two-proton and two-neutron drip lines. The right top portion shows the thickness of proton skin as a function of proton's Fermi level measured from the top of the Coulomb barrier as defined in the text. The right bottom portion shows the thickness of neutron skin versus neutron's Fermi level.

The left-hand portion of Fig. 17 shows the thickness of the proton and neutron skins in the (N, Z) plane. Note that the absolute magnitudes of this quantity depend on our specific choice of the definition of the skins but the relative differences between adjacent nuclei are rather insensitive to the definition. The increase of skin thickness along isotope and isotone chains looks monotonous. If one would fold the graph in a line $N = Z$, one could easily find a general rule that the proton skin of a proton rich nucleus is larger than the neutron skin of its mirror nucleus. This fact can be ascribed to the Coulomb repulsion between protons. However, since the proton drip line is closer to the $N = Z$ line than the neutron drip line is, proton skins are much rare than neutron skins if nuclei outside the drip lines are excluded.

The top-right and the bottom-right portions of Fig. 17 present the skin thickness of protons and neutrons, respectively. The Fermi levels are used as the abscissae. These figures include the data of not only those nuclei shown in the figure in the left-hand portion but all the calculated 1029 even-even nuclei. They also include not only the ground-state solutions but also first-excited solutions for 758 nuclei. Most of the dots are on the bottom line. From the figure in the right-bottom portion, one can see a general rule that the neutron's skin (by our definition) appears for $\lambda_n > -8\text{MeV}$ and increases linearly with λ_n at a rate of $\sim 0.3\text{fm/MeV}$. This rule is rather insensitive to the mass and applies both to ground and excited states.

For protons, the Fermi level should be measured from the top of the Coulomb barrier. Otherwise the dots do not cluster in a narrow area. We estimate the height of the barrier top as

$$E_{\text{C.B.}} = \frac{1.44Z}{1.2A^{1/3} + \Delta R} \text{ (MeV)}, \quad \Delta R = 1.0 \text{ fm}, \quad (4.4)$$

where ΔR is a parameter to designate the shift of the location of the barrier top from

the liquid-drop surface. We assume a constant value of ΔR for all the nuclei. Small changes of ΔR only translate uniformly the plotted dots. We choose $\Delta R = 1.0$ fm so that the horizontal location where the dots depart from the bottom line is roughly the same as in the graph for neutrons. The resulting behavior of the skin thickness of protons is very similar to that of the neutrons.

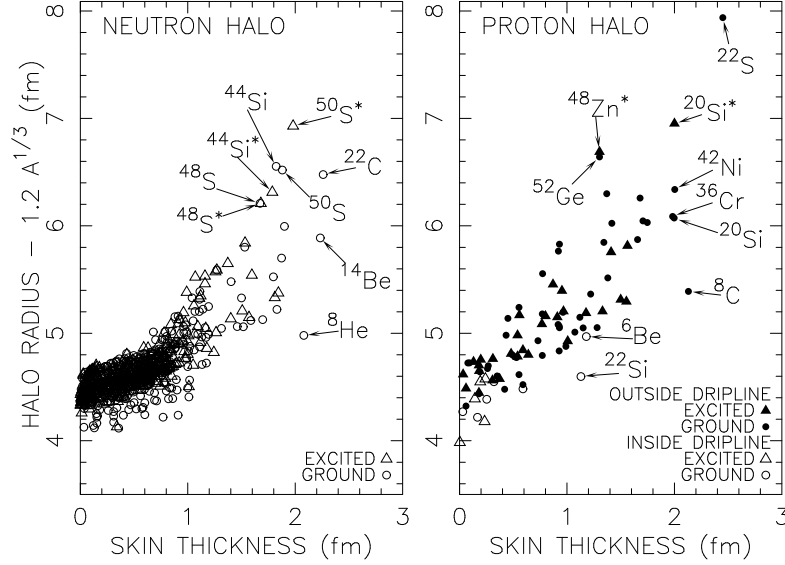


Fig. 18. The radius of the neutron (proton) halo plotted versus the thickness of the neutron (proton) skin (in the left (right) portion). Element names are printed for nuclei with large halo radius. An asterisk symbol put to the right shoulder of the element name indicates that the state is the first excited solution of the nucleus.

Fig. 18 shows “the thickness of the halo”, i.e., the radius of the halo subtracted with the liquid-drop radius $1.2A^{-1/3}$ fm. The abscissa is the thickness of neutron (proton) skin for the neutron (proton) halo. One can see that halos grow only slowly for skin thickness less than 1 fm but it expands rapidly after 1 fm. This sudden change is widely understood to be ascribed to the last occupied orbital’s spatial extension due to its small binding energy.

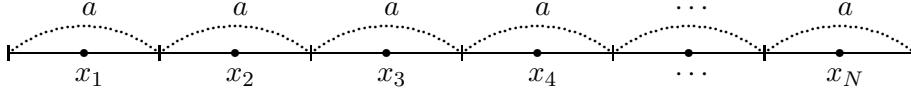
Acknowledgements

The author thanks Dr. P. Bonche, Dr. H. Flocard, and Dr. P.-H. Heenen for providing a Cartesian-mesh HF+BCS code *EV8*.¹⁹⁾ They are also grateful to Dr. T. Tachibana and Dr. K. Oyamatsu for the TUYU mass formula code, and to Dr. S. Raman for the computer file of the B(E2) \uparrow table. Most of the calculations discussed in this paper have been carried out in collaboration with Dr. S. Takahara of Kyorin University.

Appendix A

— Cartesian Mesh and the Fourier Basis —

In this Appendix we explain the origin of the surprising high accuracy of nuclear mean-field calculations with apparently coarse Cartesian meshes. It is sufficient to consider a one-dimensional space because the essence is there. We put N mesh points at $x_i = (i - \frac{1}{2})a$ ($1 \leq i \leq N$) in an interval $0 \leq x \leq Na$ as in the following illustration.



In the mesh representation, any function $\psi(x)$ defined in this interval is expressed in terms of a set of its values at the mesh points $\psi_i = \psi(x_i)$. The equation to determine $\{\psi_i\}$ is usually derived as a discrete approximation to the Schrödinger equation. An alternative point of view was presented by Baye and Heenen.⁴⁰⁾ They introduced a set of orthogonal basis functions $f_i(x)$,

$$f_i(x) = f\left(\frac{x - x_i}{a}\right), \quad f(\xi) = \frac{\sin Nak_0\xi}{N \sin ak_0\xi}, \quad k_0 = \frac{\pi}{Na}, \quad 1 \leq i \leq N. \quad (\text{A.1})$$

The shape of the above basis function is shown in Fig. 19. When $\psi(x)$ can be

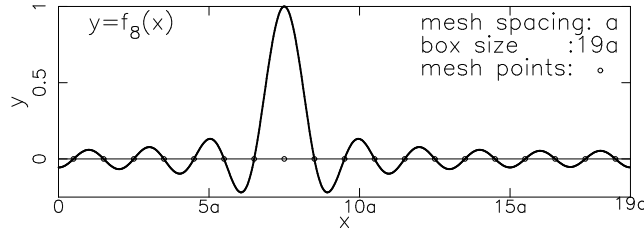


Fig. 19. The graph of a Fourier basis function $y = f_8(x)$ corresponding to the 8th mesh point for mesh spacing a and interval $19a$. All the mesh points are indicated with open circles on the $y = 0$ line.

expressed as a linear combination of $\{f_i(x)\}$, ψ_i is nothing but the coefficient of $f_i(x)$,

$$\psi(x) = \sum_{i=1}^N \psi_i f_i(x), \quad (\text{A.2})$$

owing to a property of the basis, $f_i(x_j) = \delta_{ij}$. From this point of view, one can uniquely derive the equation to determine $\{\psi_i\}$ from the variational principle in a space spanned by the trial wave functions of form (A.2) and can avoid the arbitrariness to choose a discrete approximation formula.

The expression (A.2) is equivalent to a truncated Fourier expansion with a

boundary condition $\psi(x + Na) = (-1)^{N+1}\psi(x)$ because one can write

$$f_j(x) = \frac{1}{N} \sum_{n=1}^N e^{i(2n-N-1)k_0(x-x_j)}. \quad (\text{A}\cdot 3)$$

This is the very reason why the Cartesian mesh representation provides high accuracy in nuclear calculations: The Cartesian mesh is associated with the Fourier or plane-wave basis, which is especially suitable to the atomic nucleus owing to its saturation property.

Concerning integrals, the mid-point rule is exact for the product of two wave functions,

$$\int_0^{Na} \psi^*(x)\phi(x)dx = a \sum_i \psi_i^* \phi_i, \quad (\text{A}\cdot 4)$$

where $\psi(x)$ and $\phi(x)$ are functions of form (A·2) and $\phi_i = \phi(x_i)$. For other integrands like $\psi^*(x)V(x)\phi(x)$, the mid-point rule similar to Eq. (A·4) is not exact any more. Nevertheless, one should yet use the mid-point formula rather than high-order formulae like Eq. (C·2) for the sake of high precision.

On the other hand, the expressions for derivatives are not so simple. The expression of the ν th derivative of the function defined by Eq. (A·2) at a mesh point x_i involves a full $N \times N$ matrix $D_{ij}^{(\nu)}$:

$$\left. \frac{d^\nu}{dx^\nu} \psi(x) \right|_{x=x_i} = \frac{1}{a^\nu} \sum_{j=1}^N D_{ij}^{(\nu)} \psi_j, \quad (\text{A}\cdot 5)$$

where the matrices for $\nu = 1$ and 2 are expressed respectively as

$$D_{ij}^{(1)} = \begin{cases} 0 & (i = j) \\ (-1)^{i-j} \frac{\pi}{N \sin \frac{i-j}{N} \pi} & (i \neq j) \end{cases} \quad (\text{A}\cdot 6)$$

and

$$D_{ij}^{(2)} = \begin{cases} \frac{1-N^2}{3N^2} \pi^2 & (i = j) \\ -(-1)^{i-j} \frac{2\pi^2}{N^2 \tan \frac{i-j}{N} \pi \sin \frac{i-j}{N} \pi} & (i \neq j) \end{cases}. \quad (\text{A}\cdot 7)$$

Since the evaluation of this expression seems to require a rather long computation time for the resulting precision, the code *EV8*¹⁹⁾ employs a finite-point approximation formula like Eq. (B·1) to approximate Eq. (A·5) rather than sticking to the variational picture as completely as possible.

The extension to the three-dimensional case is straightforward. A wave function is expressed by its values ψ_{ijk} at mesh points $(x_i, y_j, z_k) = ((i - \frac{1}{2})a, (j - \frac{1}{2})a, (k - \frac{1}{2})a)$ as,

$$\psi(x, y, z) = \sum_{ijk} \psi_{ijk} f_i(x) f_j(y) f_k(z). \quad (\text{A}\cdot 8)$$

It is worth noting that, for polar and cylindrical coordinates, the mesh points become non-uniform in order to make the associated bases the eigenfunctions of the kinetic energy. If one takes the radial mesh points equidistantly, the spacing must be finer than that of the three-dimensional Cartesian mesh. Meshes with 1 fm spacing are too coarse for the radius grid but fine enough for three-dimensional Cartesian mesh.

Appendix B

— Finite-Point Formulae for Numerical Differentiation —

The ν th derivative of a function $f(x)$ can be evaluated approximately by the values of the function at n mesh points as,

$$\frac{d^\nu f(x)}{dx^\nu} = \frac{1}{b_n^{(\nu)} a^\nu} \sum_{i=(n-1)/2}^{(n-1)/2} c_{ni}^{(\nu)} f(x + ai) + \mathcal{O}(a^{n-[\nu-1]_e-1}), \quad (\text{B.1})$$

where $n \geq 3$ is an odd number while $[j]_e$ means the maximum even number not exceeding j . The coefficients $c_{ni}^{(\nu)}$ and $b_n^{(\nu)}$ can be determined by approximating $f(x)$ with the polynomial in x of degree $n-1$ which coincides with $f(x)$ at the n points.

Coefficients up to the six-point formula are given in table 25.2 of Ref.⁴¹⁾ We have utilized a symbolic computation software *mathematica*⁴²⁾ to obtain the values of the coefficients of higher-order formulae, which are given in Table I.

We show in Fig. 20 the results of our calculations with which we examine the precision of the kinetic energy calculated using Eq. (B.1). The results are for one-dimensional case but can be easily applied to three-dimensional cases because the kinetic energy is divided into x , y and z components.

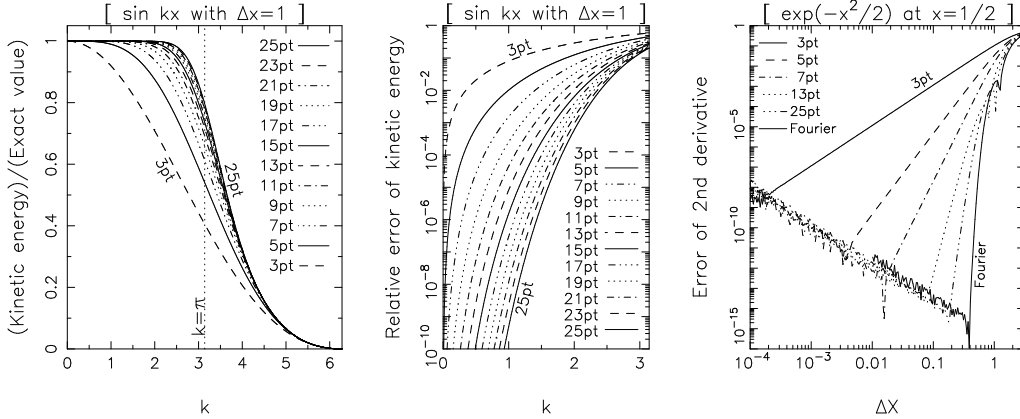


Fig. 20. Precision of finite-point numerical differentiation formulae.

In the left-hand portion of Fig. 20, the ratio of the numerically calculated value of $\int_0^{2\pi/k} \sin kx \frac{d^2}{dx^2} \sin kx dx$ to its exact value $-k\pi$ is plotted as a function of the wave number k . The mesh spacing a (expressed as Δx in the figure) is taken as 1 fm. We change k from 0 to 2π for an aesthetic reason, though $k > \pi/a = \pi \text{ fm}^{-1}$

Table I. Coefficients of the n -point approximation formulae for the ν th derivative given in Eq. (B.1). $c_{ni}^{(\nu)}$ for negative i can be obtained using a relation $c_{n,-i}^{(\nu)} = (-1)^i c_{ni}^{(\nu)}$. $c_{n0}^{(\nu)} = 0$ for odd ν .

Sign of $c_{ni}^{(\nu)}$			
	$i < 0$	$i = 0$	$i > 0$
$\nu = 1$	$(-1)^i$	0	$(-1)^{i+1}$
$\nu = 2$	$(-1)^{i+1}$		

First derivative ($\nu = 1$)

n	$b_n^{(1)}$	$ c_{ni}^{(1)} ; i = 1, 2, \dots, \frac{1}{2}(n-1)$
3	2	1
5	12	8, 1
7	60	45, 9, 1
9	840	672, 168, 32, 3
11	2520	2100, 600, 150, 25, 2
13	27720	23760, 7425, 2200, 495, 72, 5
15	360360	315315, 105105, 35035, 9555, 1911, 245, 15
17	720720	640640, 224224, 81536, 25480, 6272, 1120, 128, 7
19	12252240	11027016, 4009824, 1559376, 539784, 154224, 34272, 5508, 567, 28
21	232792560	211629600, 79361100, 32558400, 12209400, 3907008, 1017450, 205200, 29925, 2800, 126

Second derivative ($\nu = 2$)

n	$b_n^{(2)}$	$ c_{ni}^{(2)} ; i = 0, 1, 2, \dots, \frac{1}{2}(n-1)$
3	1	2, 1
5	12	30, 16, 1
7	180	490, 270, 27, 2
9	5040	14350, 8064, 1008, 128, 9
11	25200	73766, 42000, 6000, 1000, 125, 8
13	831600	2480478, 1425600, 222750, 44000, 7425, 864, 50
15	75675600	228812298, 132432300, 22072050, 4904900, 1003275, 160524, 17150, 900
17	302702400	924708642, 538137600, 94174080, 22830080, 5350800, 1053696, 156800, 15360, 735
19	15437822400	47541321542, 27788080320, 5052378240, 1309875840, 340063920, 77728896, 14394240, 1982880, 178605, 7840
21	293318625600	909151481810, 533306592000, 99994986000, 27349056000, 7691922000, 1969132032, 427329000, 73872000, 9426375, 784000, 31752

is meaningless from the point of view of the Fourier expansion. In the numerical calculation, the second derivative of $\sin kx$ is approximated by that of the $(2n+1)$ -point Lagrange polynomial, which has degree n and coincides with $\sin kx$ at $x, x \pm a, \dots, x \pm na$. The number of points is chosen as $n = 3, 5, \dots, 25$. The integral, too, is evaluated numerically but with much higher precision than that of the numerical differentiation. Hence the plotted quantity is the error of numerical differentiation, not that of integration. From this result one can see that the value of kinetic energy is always underestimated and the error becomes smaller by employing higher-order formulae.

The middle portion of Fig. 20 is the same as the left-hand portion except that the ordinate is the relative error $|(\text{ratio}) - 1|$ in logarithmic scale. One can read off from

the figure, for example, that the relative error of the kinetic energy at $k = 1.4 \text{ fm}^{-1}$ is 3.0×10^{-3} for the 9-point formula of the second derivative. The 9-point formula is used in the calculations presented in this paper. This error roughly accounts for the error of the total energy of ^{240}Pu , which is 0.5%. One can conclude that the main source of the error of the total energy is the kinetic energy.

In the right-hand portion of Fig. 20, the error of numerically evaluated values of the second derivative of a function $e^{-x^2/2}$ at $x = \frac{1}{2}$ is shown as a function of the mesh spacing a (called Δx in the figure). The numerical evaluation means the usage of the $(2n+1)$ -point Lagrange polynomial which coincides with the function $e^{-x^2/2}$ at $x = \frac{1}{2}, \frac{1}{2} \pm a, \dots, \frac{1}{2} \pm na$. The solid curve labeled as “Fourier” indicates the error of the Fourier interpolation, which coincides with the original function $e^{-x^2/2}$ at infinite number of discrete points of $x = \frac{1}{2} + na$ ($n = 0, \pm 1, \pm 2, \dots$). For plane waves with $k < \pi/a$, the Fourier interpolation gives the exact value. For functions involving higher wave-number components, as the present Gaussian function, the Fourier method does not result in the exact value. Nevertheless, as one can see from the figure, it is still much more precise than polynomial-based formulae.

In order to evaluate the derivative values at points within $\frac{1}{2}(n-1)a$ from the boundaries, one needs the values of the function beyond the boundaries. In order to obtain them one has to assume either vanishing (reflection antisymmetric) or periodic boundary conditions. A much easier method is to assume the function to be zero beyond the boundaries. However it is justified only when the function is well-damped before reaching the boundaries. Otherwise it produces a discontinuity of derivative values at the boundaries and invalidate the n -point formulae for $n \geq 3$. Usage of a cavity whose shape is not a box (rectangular parallelepiped) can be justified only for functions well-localized around the center of the cavity.

Appendix C

—— Finite-Point Formulae for Numerical Integration ——

The integral of a function $f(x)$ over an interval $0 \leq x \leq L$ can be evaluated by the values of the function at $n+1$ mesh points, $x_i = ai$ ($0 \leq i \leq n$, $a = L/n$), by approximating the function with a polynomial in x of degree n coinciding with $f(x)$ at the mesh points. Such formulae are called $(n+1)$ -point Newton-Cotes closed type integration formula and are expressed as

$$\int_0^{na} f(x)dx = a \sum_{i=0}^n \frac{\alpha_{ni}}{\beta_n} f(ai) + \mathcal{O}(a^{n+\delta}), \quad \delta = \begin{cases} 3 & (\text{even } n) \\ 2 & (\text{odd } n) \end{cases}. \quad (\text{C.1})$$

We have calculated the values of the coefficients α_{ni} and β_n in a similar method as we calculated those of the differentiation formulae. The results are given in Table II for some odd values of $n+1$.

Two-, three-, and four-point formulae are called respectively the trapezoidal rule, Simpson’s $\frac{1}{3}$ rule, and Simpson’s $\frac{3}{8}$ rule. The errors of $2k$ -point and $(2k-1)$ -point formulae are of the same order in a , $\mathcal{O}(a^{2k+1})$, for $2k \geq 4$. For this reason we listed in Table II only 2- and odd-point formulae. The coefficients of 4- to 11-point

Table II. Coefficients of Newton-Cotes closed type $(n+1)$ -point integration formulae. Values for $i > \frac{1}{2}(n+1)$ can be obtained from a relation $\alpha_{ni} = \alpha_{n,n-i}$.

$n+1$	β_n	$\alpha_{ni}; i = 0, 1, \dots, \frac{1}{2}n+1$
3	3	1, 4
5	45	14, 64, 24
7	140	41, 216, 27, 272
9	14175	3956, 23552, -3712, 41984, -18160
11	299376	80335, 531500, -242625, 1362000, -1302750, 2136840
13	5255250	1364651, 9903168, -7587864, 35725120, -51491295, 87516288, -87797136
15	2501928000	631693279, 4976908048, -5395044599, 24510099488, -46375653541, 88410851312, -117615892611, 136741069248

formulae agree with Eqs. 25.4.13 – 20 of Ref.⁴¹⁾ There is no difficulty to obtain the coefficients of formulae which involve more number of points. It should be kept in mind, however, that formulae for $n+1 \geq 9$ ($n+1 = 10$ is an exception) include negative coefficients, which cause a loss of numerical precision due to cancellations between the contributions of negative and positive coefficient points. This problem becomes more serious for larger n .

In order to apply the $(n+1)$ -point formula to a long interval, one divides the interval into m segments and applies the $(n+1)$ -point formula to each of the segments, i.e.,

$$\int_0^{mna} f(x)dx = a \sum_{j=0}^{m-1} \sum_{i=0}^n \frac{\alpha_{ni}}{\beta_n} f((i+nj)a) + \mathcal{O}(a^{n+\delta'}), \quad \delta' = \begin{cases} 2 & (\text{even } n) \\ 1 & (\text{odd } n) \end{cases}. \quad (\text{C}\cdot 2)$$

Note that points $x = jna$ ($1 \leq j \leq m-1$) appear twice in the double summation. The reason for $\delta' = \delta - 1$ is that the error of the integral over the interval length $L = mna$ is $m = L/na \propto a^{-1}$ times as large as the error on the right-hand side on Eq. (C.1).

We have calculated the precision of these formulae as a function of the mesh spacing a for three types of integrals,

$$\int_0^{2\pi} \frac{\sin 2x}{2x} dx, \quad \int_0^{2\pi} \frac{1 - \left(\frac{x}{2\pi}\right)^2}{1 + x^2} dx, \quad \int_0^{2\pi} e^{-x^2} dx, \quad (\text{C}\cdot 3)$$

as examples of three different boundary situations at $x = 2\pi$. The obtained (absolute value of the) relative errors of the integrals are shown in logarithmic scale versus the mesh spacing a ($= \Delta x$) in Fig. 21. The calculations are defined only for discrete points at $a = 2\pi/mn$. The lines drawn in the figure connect such discrete points.

In the left-hand portion of Fig. 21, the error of the n -point formula behaves as expected from Eq. (C.2) for every value of n . More-point formulae give quicker decreases of the error as the mesh spacing decreases. The noise-like error of magnitude 10^{-13} to 10^{-15} originates in the round off of real numbers into double precision (16-digit) floating numbers.

However, this is not the only situation. We now show that the convergence to the exact value is much faster for some kind of integrands and, what is more interesting is,

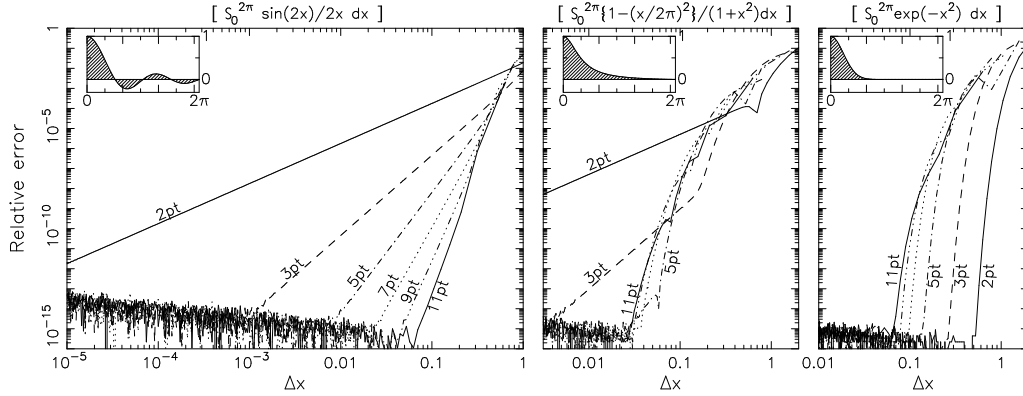


Fig. 21. Errors of numerical integral with Newton-Cotes closed type formulae. See text for explanations.

that such fast convergences become more outstanding by using low-order few-point formulae than high-order many-point ones.

The right-hand portion of Fig. 21 shows the results for a different integrand e^{-x^2} . In this case, one can see that fewer-point formulae give more accurate results than more-point formulae. The convergences are generally much faster than those in the left-hand portion of the figure.

The origin of this unexpected situation apparently in contradiction with Eq. (C-2) is the approximate periodicity of the integrand. The function e^{-x^2} in an interval $[0, 2\pi]$ can be regarded as a half wave length portion of a periodic function, which is constructed using this portion of the function by repeating reflections at the boundaries $x = 0$ and 2π . At $x = 0$ the function is reflection symmetric originally. For $x > 2\pi$ the function is redefined by a reflection symmetry requirement $f(2\pi + x) = f(2\pi - x)$. This reflection makes practically no discontinuities at $x = 2\pi$ (or between $x = \pm 2\pi$ because the period is 4π) because e^{-x^2} and its derivatives (of not extremely high order; the graph includes up to 11-point formula and thus only up to 11th derivative concerns) are close to zero at $x = 2\pi$.

The integral over $[0, 2\pi]$ is a half of the integral of thus constructed smooth periodic function over the wave length 4π . It is known that the best numerical formula for integrals of periodic functions over a wave length is the mid-point rule. The reason is often explained in terms of an asymptotic expansion. A more quantitatively accurate explanation can be given in terms of Fourier expansions, as explained in Appendix A.

Periodic functions composed of wave numbers less than π/a can be exactly integrated with the mid-point rule. The function e^{-x^2} is an approximately periodic function and its large-wave-number components are non-zero but very small. Therefore the mid-point rule is the most precise formula for this integrand. The 2-point formula is the same as the mid-point rule in the present situation

The $(n + 1)$ -point formulae can be regarded as a summation of n similar results of 2-point formula with mesh spacing of na . The curve of the error of the 3-point formula resembles to that of the 2-point formula except it is shifted leftward by a

factor $(2-1)/(3-1) = \frac{1}{2}$. Similarly, the horizontal distance between the curves for 3- and 5-point formulae is also calculated as $(3-1)/(5-1) = \frac{1}{2}$.

We have searched for an integrand which gives rise to an intermediate situation between the left-hand and the right-hand portions of Fig. 21. A function which serves for this aim is $\{1 - (x/2\pi)^2\} / (1 + x^2)$. The middle portion of Fig. 21 shows the error of the integral for this integrand. One can see that the situation is like that of the left-hand (right-hand) portion of the figure for small (large) $a (= \Delta x)$. The most precise formula changes with the mesh spacing: It is the 2-point formula for $a > 0.3$, the 3-point formula for $0.08 < a < 0.3$, and the 5-point formula for $a < 0.08$.

This change can be understood as follows. With large a , the precision is so low that the discontinuity at $x = 2\pi$ looks too small to invalidate the approximation of the periodicity. Consequently, the error behaves like a parabola as in the right-hand portion of the figure. With small a , the precision is so high that the discontinuity looks large enough to violate the periodicity. Thus the error behaves linearly as in the left-hand portion of the figure.

In the nuclear mean-field calculations, the integrands are not exactly periodic. However, the situation resembles that of the right-hand portion of Fig. 21 for nuclei whose Fermi levels are not very shallow, because the wave functions are well damped before reaching to the boundaries. This is why we employ the mid-point rule in our calculations.

There are also modified types of Newton-Cotes formulae, in which the coefficients are different from 1 only near the boundaries:

$$\int_0^{Na} f(x)dx = a \sum_{i=0}^N \frac{\alpha'_{Nni}}{\beta'_n} f(ai) + \mathcal{O}(a^{n+\delta'}), \quad \delta' = \begin{cases} 2 & (\text{even } n) \\ 1 & (\text{odd } n) \end{cases}, \quad (\text{C.4})$$

with

$$\alpha'_{N,n,i} = \alpha'_{N,n,N-i} \quad (0 \leq i \leq n), \quad (\text{C.5})$$

$$\alpha'_{Nni} = \beta'_n \quad (n+1 \leq i \leq N-n-1). \quad (\text{C.6})$$

We temporarily call the above equations the boundary-correction type formulae in this paper. We have calculated the values of the coefficients α'_{Nni} and β'_n in a similar manner as we treated Eq. (C.1). Table III gives the values of the coefficients. For $(n+1)$ -point formula, the coefficients are different from one only for $n+1$ points near each ends of the integration interval. Only in the 2-point formula, which is identical to the extended trapezoidal rule, the end points alone have a non-unit coefficient. We give both $2k$ -point and $(2k-1)$ -point formulae in the table. Although their errors are of the same order in a , the former seems slightly more precise than the latter in some test calculations. We have found only the 3-point formula in literature. It is Eq. (4.1.14) of Ref.⁴³⁾ Although the formulae are identical, the derivation is quite different.

Boundary-correction type formulae will be useful to treat deeply bound, weakly bound, and positive-energy orbitals in a single framework. With the formulae, the deeply bound orbitals are treated with the high precision of the mid-point rule for

Table III. Coefficients of Boundary-correction type $(n + 1)$ -point integration formulae.

$n + 1$	β'_n	$\alpha'_{Nni}; i = 0, 1, \dots, n$
2	2	1, 2
3	24	9, 28, 23
4	24	8, 31, 20, 25
5	1440	475, 1902, 1104, 1586, 1413
6	1440	459, 1982, 944, 1746, 1333, 1456
7	120960	36799, 176648, 54851, 177984, 89437, 130936, 119585
8	120960	35584, 185153, 29336, 220509, 46912, 156451, 111080, 122175
9	7257600	2082753, 11532470, 261166, 16263486, -1020160, 12489922, 5095890, 7783754, 7200319
10	7257600	2034625, 11965622, -1471442, 20306238, -7084288, 18554050, 1053138, 9516362, 6767167, 7305728
11	958003200	262747265, 1637546484, -454944189, 3373884696, -2145575886, 3897945600, -1065220914, 1942518504, 636547389, 1021256716, 952327935
12	958003200	257696640, 1693103359, -732728564, 4207237821, -3812282136, 6231334350, -3398609664, 3609224754, -196805736, 1299041091, 896771060, 963053825
13	5230697472000	1382741929621, 9535909891802, -5605325192308, 28323664941310, -32865015189975, 53315213499588, -41078125154304, 39022895874876, -13155015007785, 12465244770050, 3283609164916, 5551687979302, 5206230892907
14	5230697472000	1360737653653, 9821965479386, -7321658717812, 34616887868158, -48598072507095, 81634716670404, -78837462715392, 76782233435964, -41474518178601, 28198302087170, -3009613761932, 7268021504806, 4920175305323, 5252701747968
15	62768369664000	16088129229375, 121233187986448, -109758975737401, 502985565327936, -823993097730133, 1461175500619600, -1668277571373981, 1746664157478912, -1219701572786787, 819644306759856, -276710928642475, 174692180291008, 37176466501689, 66395850785776, 62528161418177

periodic integrands while the weakly bound and positive-energy orbitals are treated with less precise but still high-precision $(n + 1)$ -point formula.

References

- 1) C.F. von Weizsäcker, Z. Phys. **96** (1935) 431.
- 2) H.A. Bethe and R.F. Bacher, Rev. Mod. Phys. **8** (1936) 82.
- 3) P. Ring and P. Schuck, *The nuclear many-body problem* (Springer, New York, 1980)
- 4) G. Audi and A.H. Wapstra, Nucl.Phys. **A565** (1993) 1.
- 5) G. Audi and A.H. Wapstra, Nucl.Phys. **A595** (1995) 409;
<http://www.nndc.bnl.gov/nndcscr/masses/>
- 6) T. Tachibana, M. Uno, M. Yamada, and S. Yamada, Atomic Data Nucl. Data Tables **39** (1988) 251.
- 7) H. Koura and M. Yamada, Nucl. Phys. **A671** (2000) 96.
- 8) H. Koura, M. Uno, T. Tachibana, and M. Yamada, Nucl. Phys. **A674** (2000) 47.
- 9) J. Duflo and A.P. Zuker, Phys. Rev. **C52** (1995) R23.
- 10) M. Uno, proc. Models and Theories of the Nuclear Mass, RIKEN Review **26** (2000) 38.
- 11) P. Möller, J.R. Nix, W.D. Myers, and W.J. Swiatecki, Atomic Data Nucl. Data Tables **59**

- (1995) 185.
- 12) Y. Aboussir, J.M. Pearson, A.K. Dutta, and F. Tondeur, Nucl. Phys. **A549** (1992) 155; Atomic Data Nucl. Data Tables **61** (1995) 127.
- 13) N. Tajima, S. Takahara, and N. Onishi, Nucl. Phys. **A603** (1996) 23-49; <http://serv.apphy.fukui-u.ac.jp/~tajima/hfs3/index.html> .
- 14) F. Tondeur, S. Goriely, J.M. Pearson, and M. Onsi, Phys. Rev. **C62** (2000) 024308.
- 15) S. Goriely, F. Tondeur, and J.M. Pearson, to appear in Atomic Data and Nuclear Data Tables.
- 16) K. Sumiyoshi, D. Hirata, I. Tanihata, Y. Sugahara, and H. Toki, RIKEN Review **14** (1996) 25.
- 17) D. Vautherin, Phys.Rev.**C7** (1973) 296.
- 18) J. Dechargé and D. Gogny, Phys. Rev. **C21** (1980) 1568.
- 19) P. Bonche, H. Flocard, P.-H. Heenen, S.J. Krieger, and M.S. Weiss, Nucl. Phys. **A443** (1985) 39.
- 20) I. Tanihata et al., Phys. Rev. Lett. **55** (1985) 276.
- 21) N. Tajima, N. Onishi, S. Takahara, Nucl. Phys. **A588** (1995) 215c-220c.
- 22) S. Takahara, N. Tajima, and N. Onishi, Nucl. Phys. **A642** (1998) 461-479.
- 23) T.H.R. Skyrme, Phil. Mag. **1** (1956) 1043.
- 24) D. Vautherin and D.M. Brink, Phys. Rev. **C5** (1972) 626.
- 25) N. Tajima, P. Bonche, H. Flocard, P.-H. Heenen, and M.S. Weiss, Nucl. Phys. **A551** (1993) 434.
- 26) M. Beiner, H. Flocard, Nguyen van Giai, and P. Quentin, Nucl.Phys. **A238** (1975) 29.
- 27) M. Hamermesh, *Group theory and its application to physical problems* (Addison-Wesley, 1964), chap. 2-7.
- 28) N. Tajima, proc. Innovative Computational Methods in Nuclear Many-Body Problems, Osaka, Japan, 1997, edited by H. Horiuchi et al., (1998) World Scientific (Singapore) , p. 343.
- 29) N. Tajima, proc. Models and Theories of the Nuclear Mass, RIKEN Review **26** (2000) 87.
- 30) S. Raman, C.H. Malarkey, W.T. Milner, C.W. Nestor, JR., and P.H. Stelson, Atomic Data Nucl. Data Tables **36** (1987) 1.
- 31) S. Raman, J.A. Sheikh, and K.H. Bhatt, Phys. Rev. **C52** (1995), 1380.
- 32) J. Bartel, P. Quentin, M. Brack, C. Guet, and H.-B. Hakansson, Nucl.Phys. **A386** (1982) 79.
- 33) Nguyen Van Giai and H. Sagawa, Phys. Lett **B106**, 379 (1981).
- 34) A.B. Volkov, Nucl. Phys. **74** (1965) 33.
- 35) G. Leander, S.E. Larsson, Nucl. Phys. **A239** (1975) 93.
- 36) Y. Kanada-En'yo and H. Horiuchi, Prog. Theor. Phys. **93** (1995) 115.
- 37) L. Zamick, D.C. Zheng, J.A. Caballero, E. Moya de Guerra, Ann. Phys. **212** (1991) 402.
- 38) Naoki Tajima and Norifumi Suzuki, nucl-th/0103061.
- 39) N. Fukunishi, T. Otsuka, and I. Tanihata, Phys. Rev. **C48** (1993) 1648.
- 40) D. Baye and P.-H. Heenen, J. Phys. **A19** (1986) 2041.
- 41) Handbook of mathematical functions, 9th printing, ed. M. Abramowitz and I.A. Stegun, Dover, N.Y. (1970).
- 42) S. Wolfram, *Mathematica, a System for Doing Mathematics by Computer* (Addison-Wesley, 1991).
- 43) W.H. Press, S.A. Teukolsky, W.T. Vetterling, and B.P. Flannery *Numerical Recipes in C* (Cambridge Univ. Press, 1992).

This paper has been published in Progress of Theoretical Physics Supplement No. 142 (2001) on Physics of Unstable Nuclei, pp. 265-296.
The author converted the source file of the paper into Latex2e format in order to include PostScript figures and then uploaded it to the e-print archive *arXiv* on July 22, 2003.